Coordinated Motion of Epithelial Layers on Curved Surfaces

L. Happel[1] and A. Voigt[1,2,3]
[1]Institute of Scientific Computing, TU Dresden, 01062 Dresden, Germany
[2]Center for Systems Biology Dresden, Pfotenhauerstr. 108, 01307 Dresden, Germany
[3]Cluster of Excellence, Physics of Life, TU Dresden, Arnoldstr. 18, 01307 Dresden, Germany

(Received 3 July 2023; accepted 21 December 2023; published 13 February 2024)

Coordinated cellular movements are key processes in tissue morphogenesis. Using a cell-based modeling approach we study the dynamics of epithelial layers lining surfaces with constant and varying curvature. We demonstrate that extrinsic curvature effects can explain the alignment of cell elongation with the principal directions of curvature. Together with specific self-propulsion mechanisms and cell-cell interactions this effect gets enhanced and can explain observed large-scale, persistent, and circumferential rotation on cylindrical surfaces. On toroidal surfaces the resulting curvature coupling is an interplay of intrinsic and extrinsic curvature effects. These findings unveil the role of curvature and postulate its importance for tissue morphogenesis.

DOI: 10.1103/PhysRevLett.132.078401

Geometry, and in particular local curvature, influences biological systems at various length scales [1]. One example associated with curved epithelial layers is collective rotation. Persistent and synchronous rotation on a sphere has been observed *in vivo* [2–6], *in vitro* [7–10], and *in silico* [6,11]. These phenomena differ significantly from collective behavior in flat space and are attributed to the geometric and topological properties of the sphere. Nevertheless, the underlying mechanisms that trigger such collective rotation remain unclear even for surfaces as simple as a sphere, not to mention the curved environments that epithelial tissues encounter during morphogenesis. To better understand how curvature influences epithelial layers we consider two prototypical geometries which allow for validation for specific cell types [12,13].

At the single cell level it has been shown that cells sense and respond to curvature [14–16], essentially by regulating the transcellular network architecture [17–19] and aligning the filaments with the principal curvature directions [18]. Experimental realizations furthermore show a dependence on cell type, while, e.g., filaments of fibroblasts align with the minimal curvature direction [16,18], the elongation direction of MDCK cells aligns with the maximal curvature direction [18]. Also the nucleus plays a role and cell migration on curved surfaces is shown to follow the path of least nuclear mechanical stress [14,15]. These phenomena, which describe the response to cell-scale curvature, are termed curvotaxis [14] and can be extended to collective cell behavior on curved surfaces. Coordinated rotation has been associated with the alignment of filaments with principal curvature directions, cell-cell adhesion, and apical-basal polarity [9,10]. In [12] cylindrical epithelia of MDCK cells are considered. The results indicate that proper cell-cell adhesion is essential, as well as aligned cellular polar order. This alignment is again in the principal curvature directions. In contrast, the orientation of the actin network does not seem to be essential for collective rotation. Also geometries with varying curvature, e.g., toroidal surfaces have been considered [13]. However, in [13] only cell elongation is addressed.

In this Letter we propose a minimal cell-based surface model that reproduces these effects for MDCK cells. Two-dimensional vertex models, e.g., [20–22] and multiphase field models [23–29] have been successfully used to simulate epithelial tissue in flat space. Extensions to curved surfaces are still rare, see [6,30] for vertex models and [11] for multiphase field models considered on a sphere. None of these approaches account for extrinsic curvature contributions. These terms, which somehow translate the three-dimensional nature of a thin layer, for an epithelial layer, e.g., the difference between the apical and basal side, into an effectively two-dimensional framework on the curved surface, will be shown to be essential to model the curvature effects discussed above. Extrinsic curvature effects are well established in the theory of surface liquid crystals [31,32]. These theories force the director field to be tangential to the surface and the corresponding free energies contain coupling terms between the director field and the principal curvature directions of the shape operator [31–34]. These terms follow naturally if the energies are derived as thin film limits from three-dimensional theories [33–35] and have shown various implications on phase transitions [36], active nematodynamic flows [37–39], and shape deformations [40].

We consider a multiphase field model that allows for cell deformations, local cellular rearrangements, and detailed cell-cell interactions, as well as extrinsic curvature coupling [29,41]. We consider two-dimensional phase field variables

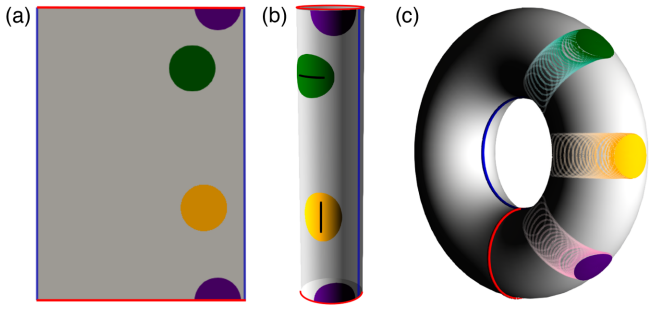

FIG. 1. Geometries and cell shapes. Red and blue lines mark periodic boundaries, which are glued together in (b) and (c) (not to scale). Three individual cells are shown in their equilibrium configuration in (a) and (b). The colors correspond to the parameter Ec which models extrinsic curvature effects, see Eq. (3). $\mathrm{Ec} = 0$ (purple) leads to a (geodesic) circle on both geometries. $\mathrm{Ec} > 0$ (green) favors an alignment in direction of maximum absolute curvature and $\mathrm{Ec} < 0$ (yellow) an alignment in direction of minimal absolute curvature. The elongation is marked and enhanced for visibility. On toroidal surfaces cell shapes depend on position. In (c) trajectories and final positions and shapes of the cells are shown. The effect of extrinsic curvature is not visible. All shapes are obtained by solving Eq. (1) with $v_0 = 0$.

$\phi_i(\mathbf{x}, t)$ one for each cell, with $\mathbf{x}$ defined on the surface $\mathcal{S}$. Values of $\phi_i = 1$ and $\phi_i = -1$ denote the interior and exterior of a cell. The cell boundary is implicitly defined as the zero-level set of ϕ_i. We consider various topologically equivalent surfaces $\mathcal{S}$, see Fig. 1. The dynamics for each ϕ_i reads

$$\partial_t \phi_i + v_0(\mathbf{v}_i \cdot \nabla_{\mathcal{S}} \phi_i) = \Delta_{\mathcal{S}} \frac{\delta F}{\delta \phi_i}, \tag{1}$$

for $i = 1, \ldots, N$, where N denotes the number of cells. F is a free energy and $\mathbf{v}_i$ a vector field used to incorporate activity, with a self-propulsion strength v_0. The operators $\nabla_{\mathcal{S}}$ and $\Delta_{\mathcal{S}}$ denote the covariant derivative and Laplace-Beltrami operator on $\mathcal{S}$, respectively. All quantities are nondimensional quantities. As in previous studies [11,25,29,42–44], we consider conserved dynamics.

The free energy reads $F = F_{\mathrm{CH}} + F_{\mathrm{EC}} + F_{\mathrm{IN}}$. The first contribution is a (de Gennes-)Cahn-Hilliard energy [45,46]

$$F_{\mathrm{CH}} = \sum_{i=1}^{N} \frac{1}{\mathrm{Ca}} \int_{\mathcal{S}} \frac{1}{G(\phi_i)} \left(\frac{\epsilon}{2} \|\nabla_{\mathcal{S}} \phi_i\|^2 + \frac{1}{\epsilon} W(\phi_i) \right) d\mathcal{S},$$

which stabilizes the interface, with $W(\phi_i) = \frac{1}{4}(1 - \phi_i^2)^2$ a double-well potential, ϵ a small parameter determining the width of the diffuse interface and $1/G(\phi_i)$ a de Gennes coefficient. This term does not influence the asymptotic limit ($\epsilon \to 0$) [45] but helps to keep $-1 \le \phi_i \le 1$, which becomes important on curved surfaces [46]. We consider $G(\phi_i) = \frac{3}{2}|1 - \phi_i^2|$. Ca is the capillary number. This covariant formulation only accounts for intrinsic curvature effects. Minimizing this energy by solving Eq. (1) with $v_0 = 0$ on a cylindrical surface leads to a geodesic circle with no preferred orientation, see Fig. 1 (purple cell). This does not resample the observed properties of single cells [18].

We associate a director field with the cell shape. In flat space this has been considered in [26,29]. Adapting the definition to the surface we obtain the surface Q-tensor fields

$$\mathbf{q}_i = \begin{pmatrix} \int_{\mathcal{S}} \frac{(\partial_{\mathbf{t}_2}\phi_i)^2 - (\partial_{\mathbf{t}_1}\phi_i)^2}{2} d\mathcal{S} & \int_{\mathcal{S}} -\partial_{\mathbf{t}_1}\phi_i \partial_{\mathbf{t}_2}\phi_i d\mathcal{S} \\ \int_{\mathcal{S}} -\partial_{\mathbf{t}_1}\phi_i \partial_{\mathbf{t}_2}\phi_i d\mathcal{S} & \int_{\mathcal{S}} \frac{(\partial_{\mathbf{t}_1}\phi_i)^2 - (\partial_{\mathbf{t}_2}\phi_i)^2}{2} d\mathcal{S} \end{pmatrix},$$

where $\mathbf{t}_1(\mathbf{x})$ and $\mathbf{t}_2(\mathbf{x})$ denote orthonormal vectors of the tangent plane at $\mathbf{x} \in \mathcal{S}$, which are related by parallel transport to the principal curvature directions in the center of mass of the cell i, see Supplemental Material [47] for details, which includes Refs. [48,49]. Together with $\boldsymbol{\nu}(\mathbf{x})$, the outward-pointing normal to the surface $\mathcal{S}$, they define the Darboux frame. The eigenvectors of the tensor fields $\mathbf{q}_i$ correspond to the direction of largest elongation and contraction and the corresponding eigenvalues measure the degree of deformation. Using these directions to define director fields $\mathbf{d}_i$ allows us to associate nematic order to the epithelial tissue [11,26,29,50]. In our case $\mathbf{q}_i$ and $\mathbf{d}_i$ are tangential tensor and vector fields, respectively. Coarse-grained quantities of the surface Q-tensor fields $\mathbf{q}$ and the director fields $\mathbf{d}$ are considered in surface liquid crystal models and related by $\mathbf{q} = S(\mathbf{d} \otimes \mathbf{d} - \frac{1}{2}\mathbf{g})$ [36], where S is a nematic order parameter and $\mathbf{g}$ is the metric of the surface $\mathcal{S}$. Already in typical one-constant approximations of the corresponding surface energies, if derived as a thin film limit from the corresponding 3D models, additional geometric coupling terms occur [31–34]. In case of the surface Frank-Oseen model the term of interest reads

$$\|\nabla_C \mathbf{d}\|^2 = \|\nabla_{\mathcal{S}} \mathbf{d}\|^2 + \langle \boldsymbol{\nu} \otimes \boldsymbol{B}\mathbf{d}, \boldsymbol{\nu} \otimes \boldsymbol{B}\mathbf{d} \rangle, \tag{2}$$

where $\boldsymbol{B} = -\nabla_P \boldsymbol{\nu}$ denotes the shape operator and $\langle \cdot, \cdot \rangle$ the scalar product on $\mathcal{S}$ [51]. Thereby ∇_C denotes the Guenther derivative and ∇_P the surface tangential gradient, see Supplemental Material [47]. There are various physical implications resulting from the choice of derivative, see [36] for an overview. Relevant to our case is only the alignment of $\mathbf{d}$ with principal curvature directions resulting from the second summand in Eq. (2). This coupling term has been added in an *ad hoc* manner in [37] to account for linear curvature contributions in surface active nematodynamics. We consider it in the phase field context for each cell and define the extrinsic curvature part of the free energy by

$$F_{\mathrm{EC}} = \mathrm{Ec} \sum_{i=1}^{N} \int_{\mathcal{S}} \langle \boldsymbol{\nu} \otimes \boldsymbol{B} \nabla_{\mathcal{S}} \phi_i, \boldsymbol{\nu} \otimes \boldsymbol{B} \nabla_{\mathcal{S}} \phi_i \rangle \mathrm{d}\mathcal{S}, \quad (3)$$

where the parameter Ec determines the preferred direction and strength of this geometric coupling. We furthermore use that the integral mean of $\nabla_{\mathcal{S}} \phi_i$ is orthogonal to the elongation of the cell and is thus related to $\mathbf{d}_i$. While F_{EC} can become negative, the area conservation of ϕ_i and F_{CH} guarantee a well-posed problem within reasonable parameter settings. Figure 1 shows the effect of F_{CH} and F_{EC} on a single cell on different geometries if $v_0 = 0$. While the shape is independent on position in flat space and on cylinders, both having zero Gaussian curvature ($K = 0$) and being ruled surfaces, the shape depends on position on the torus. Here, F_{CH} can be reduced by moving the cell towards regions of maximal K. F_{EC} with $\mathrm{Ec} > 0 (< 0)$ deforms the cell from elongation in toroidal (poloidal) direction in regions of lowest K, inside, to elongation in poloidal (toroidal) direction in regions of highest K, outside, if the absolute maximal principal curvature direction changes from inside to outside. Further details are provided in the Supplemental Material [47]. However, the influence of F_{EC} is less pronounced on toroidal surfaces as the difference between the magnitude of the principal curvature directions is smaller than on the cylindrical surfaces.

The energy component F_{IN} accounts for interaction between cells. We define $\psi_i = \frac{1}{2}(\phi_i + 1)$. A common way to model repulsive and attractive forces is

$$F_{\mathrm{IN}} = \frac{1}{\mathrm{In}} \sum_{i=1}^{N} \sum_{j \neq i} \int_{\mathcal{S}} \underbrace{a_{\mathrm{rep}} \psi_i^2 \psi_j^2 - a_{\mathrm{att}} \|\nabla_{\mathcal{S}} \psi_i\|^2 \|\nabla_{\mathcal{S}} \psi_j\|^2}_{:= f_{\mathrm{IN}}} d\mathcal{S},$$

with interaction strength In and coefficients a_{rep} and a_{att}; see [24,52] for the corresponding form in flat space. We modify this formulation and consider the equilibrium condition $(\epsilon/2)\|\nabla_{\mathcal{S}} \phi_i\|^2 \approx (1/\epsilon) W(\phi_i)$ resulting from the tanh-profile of ϕ_i and approximate $a_{\mathrm{att}} \|\nabla_{\mathcal{S}} \psi_i\|^2 \|\nabla_{\mathcal{S}} \psi_j\|^2 \approx \tilde{a}_{\mathrm{att}} W(\phi_i) W(\phi_j)$, with the rescaled coefficient $\tilde{a}_{\mathrm{att}}$. This leads to the numerically more appropriate form without derivatives, where

$$f_{\mathrm{IN}} = \tilde{a}_{\mathrm{rep}} (\phi_i + 1)^2 (\phi_j + 1)^2 - \tilde{\tilde{a}}_{\mathrm{att}} (\phi_i^2 - 1)^2 (\phi_j^2 - 1)^2$$

with rescaled coefficients $\tilde{a}_{\mathrm{rep}}$ and $\tilde{\tilde{a}}_{\mathrm{att}}$, as in [25,53–55]; see Supplemental Material [47] for the resulting short-range interaction potential.

Activity is incorporated by self-propulsion defining $\mathbf{v}_i$. There are various possibilities, which differ by complexity, ranging from random motion [56] to considering mechanochemical subcellular processes [24,43] and physical implications, e.g., polarity and velocity alignment and contact inhibition [57], see [29] for a comparison. Here we define $\mathbf{v}_i = \cos(\theta_i)\mathbf{e}_1^i + \sin(\theta_i)\mathbf{e}_2^i$ with the angle θ_i which is controlled by rotational noise $d\theta_i(t) = \sqrt{2D_r} dW_i(t)$ with diffusivity D_r and a Wiener process W_i and the local orthonormal coordinate system $(\mathbf{e}_1^i, \mathbf{e}_2^i)$ in the tangent plane of the center of mass of cell i. We consider an elongation model with $\mathbf{e}_1^i$ pointing in the direction of largest elongation, similar to the approach considered in flat space in [26]. In each time step the preferred direction of movement is set by the largest elongation with some noise centered around this orientation. Collective motion results from the deformability of the cells [58,59]. In the current setting all cells have the same size, cell growth and division are neglected.

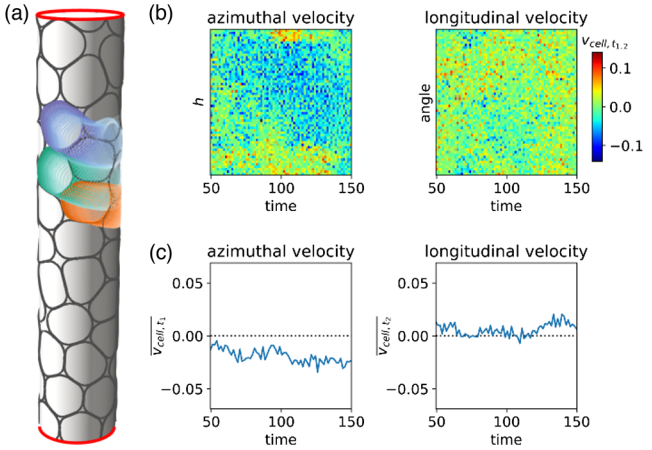

FIG. 2. Evolution on a cylinder. (a) Time instance of the evolution together with overlayed cell shapes ($\phi_i = 0$) and cells at previous time steps for three cells. For corresponding movie see Supplemental Material [47]. (b) and (c) Kymographs and graphs displaying the average velocities of the cells from (a) in azimuthal and longitudinal directions as function of time.

The problem is solved numerically using surface finite elements [51,60] and the parallelization concept introduced in [61]; see Supplemental Material [47] for details, which includes Refs. [62–67].

We consider three cylindrical surfaces with equal surface area $|\mathcal{S}|$ but different curvature and 60 equally sized cells with a packing fraction of 90% placed on them with random initial direction of movement. For geometric quantities and parameters see Supplemental Material [47]. Figure 2 shows data for one cylinder and $\mathrm{Ec} > 0$, clearly indicating collective rotation, consistent with the experiments for MDCK cells in [12].

All simulations on cylindrical surfaces are summarized in Fig. 3. We consider each cell within a time frame after an initialization phase used to randomize the cell ordering and plot the distribution of their orientation and direction of movement with respect to the angle with the longitudinal direction for three different simulations, see Supplemental Material [47] for details. The color coding corresponds to the magnitude of the averaged velocity. Without extrinsic curvature contribution [$\mathrm{Ec} = 0$, see Figs. 3(d)–3(f)] no clear trend is visible for any preferred direction of

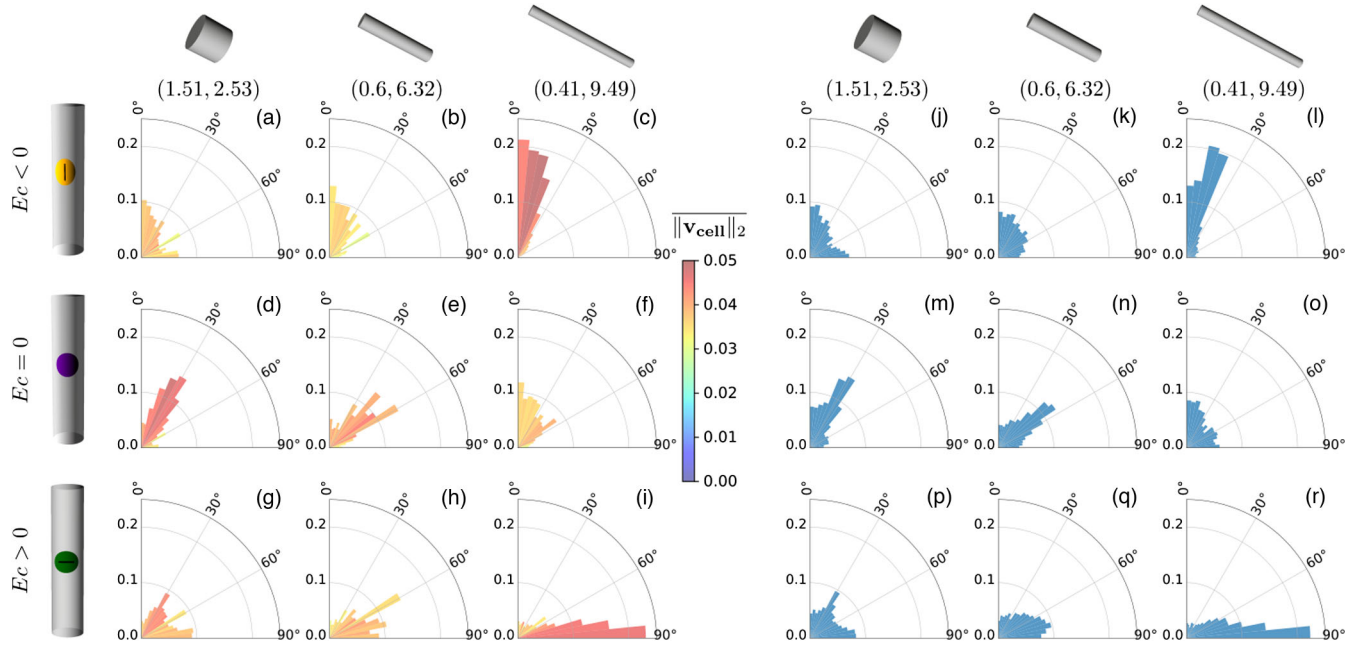

FIG. 3. Distribution of direction of motion and elongation direction on cylindrical surfaces $(r_{\text{Cyl}}, h_{\text{Cyl}})$. The angle between longitudinal direction and direction of movement or elongation direction is used as angular coordinate and the ratio of cells with this property as radial coordinate. (a)–(i) Direction of movement color coded by mean velocity, (j)–(r) direction of elongation. The data are averaged over time and three simulations for each configuration.

elongation or movement. The preference for 30° and 60° in (d) and (e), can be associated with a size constraint resulting from the high packing fraction. These numbers correspond to the equilibrium configuration of a hexagonal packing of circles. Analyzing the neighbor distribution (not shown) confirms a more dominated hexagonal packing compared with Fig. 3(f), for which the direction of movement is more distributed. For $\text{Ec} < 0$ and $\text{Ec} > 0$ the cells collectively elongate and move in the longitudinal and azimuthal direction, respectively. Any size constraint is overcome by the complex interaction of cells with curvature and each other. Increasing curvature enhances these effects. This is associated with stronger elongation, more pronounced movement in longitudinal or azimuthal direction, and increased velocity, see Figs. 3(a)–3(c) and 3(g)–3(i). The detailed data in Fig. 2 correspond to (h). Corresponding data for (a)–(i) are provided in Supplemental Material [47]. While the effect of extrinsic curvature is rather small for single cells, it is enhanced in coordinated motion leading to qualitatively different behavior. However, the enhancement of the elongation with principal curvature directions also strongly depends on the self-propulsion mechanism. Corresponding results for a random model, where $\mathbf{e}_1^i$ is chosen as the direction of the velocity vector from the last time step, which can be considered as a generalization of active Brownian particles on surfaces to deformable objects [56], are shown in Supplemental Material [47]. For the considered parameters this mechanism leads to a preferred elongation direction only for the cylindrical surfaces with the strongest curvature $(r_{\text{Cyl}}, h_{\text{Cyl}}) = (0.41, 9.49)$, but to no tendency for collective motion in the azimuthal or longitudinal direction.

On toroidal surfaces curvature varies along the poloidal direction, see Supplemental Material [47]. As seen for a single cell, this has consequences for cell shape and position. We consider the same setting on two toroidal surfaces of equal area with 144 cells. Figure 4 summarizes the results. As in Fig. 3 we plot the distribution of the direction of movement and the elongation direction. The angle is with respect to the poloidal direction. On both surfaces the toroidal direction is the preferred direction of movement and elongation for $\text{Ec} < 0$, see Figs. 4(a), 4(b), 4(g), and 4(h) and the poloidal direction is the preferred direction of movement and elongation for $\text{Ec} > 0$, see Figs. 4(e), 4(f), 4(k), and 4(l). These tendencies are more pronounced for the torus with $(R_T, r_t) = (1.81, 0.81)$. Here the maximal absolute principal curvature direction is always the poloidal direction, while for the torus with $(R_T, r_T) = (1.35, 1.08)$ it varies from the toroidal direction (inside) to the poloidal direction (outside). This change in direction leads to preferred elongation and movement directions depending on position. In both cases varying Gaussian curvature impedes the emergence of collective motion. The difference in magnitude between the principal curvature values is smaller if compared with the cylindrical surfaces. In addition, collective movement in the poloidal direction is simply restricted by the geometry. These effects can explain the observed behavior of a preferred direction of movement and elongation, but no collective motion on the torus.

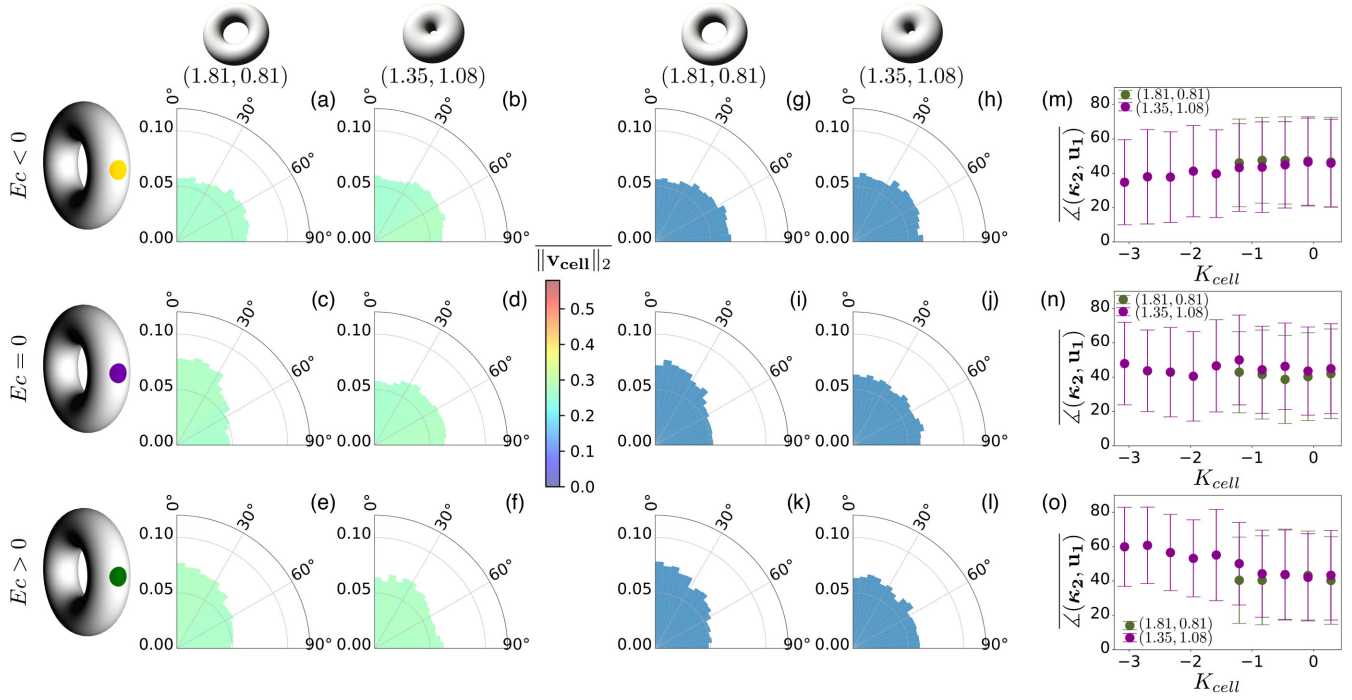

FIG. 4. Distribution of direction of motion and elongation direction on toroidal surfaces (R_T, r_T). The angle between the poloidal direction and direction of movement or elongation direction is used as an angular coordinate and the ratio of cells with this property as a radial coordinate. (a)–(f) Direction of movement color coded by mean velocity, (g)–(l) direction of elongation. The data are averaged over time and three simulations for each configuration. (m)–(o) Angle of elongation direction as a function of Gaussian curvature averaged over the area of the cell K_{cell}.

We next consider the elongation as a function of K, see Figs. 4(m)–4(o). While we do not see an effect for the torus with $(R_T, r_T) = (1.81, 0.81)$, for the torus with $(R_T, r_T) = (1.35, 1.08)$ there is a slight dependency of the elongation direction on K_{cell} for $\mathrm{Ec} < 0$ and $\mathrm{Ec} > 0$. For $\mathrm{Ec} > 0$ it agrees, at least qualitatively, with measurements for MDCK cells on toroidal surfaces within the region of negative K [13]. Quantitative differences can be associated with significantly different numbers of cells, different measurement techniques and possible influences of the considered geometry in [13]. The direction of movement has a less pronounced dependency on K, see Supplemental Material [47].

Incorporating extrinsic curvature contributions into a cell-based surface multiphase field model allows us to effectively resolve the three-dimensional nature of epithelial layers, e.g., the difference between the apical and basal side. This reveals essential effects of curvature on single cells and their collective motion. The alignment of cells with principal curvature directions leads under appropriate propulsion mechanisms and cell-cell interactions to collective motion on specific geometries. On cylindrical surfaces this can lead to long-term changes from a quiescent state to spontaneous collective rotation, as observed *in vitro* for MDCK cells [12]. Cylindrical surfaces are not only special mathematical objects, they are representative of many epithelial tissues, such as tubular vessels, ranging from small capillaries to large arteries, tubular glands, and ducts [16,18]. On more general surfaces with varying K the geometric effect on the collective behavior is a competition of intrinsic and extrinsic curvature contributions. Both couplings vastly increase the range of tissue parameters to control the flow of the epithelial layer. Combining this with shape changes induced by these tangential flows, as considered in coarse-grained models for fluid deformable surfaces [68–70], has the potential to transform our understanding of morphogenesis.

Data and simulation code are available upon reasonable request.

This work was funded by DFG within FOR3013. We further acknowledge computing resources at FZ Jülich under Grant No. PFAMDIS and at ZIH under grant WIR.

[1] B. Schamberger *et al.*, Curvature in biological systems: Its quantification, emergence, and implications across the scales, Adv. Mater. **35**, 2206110 (2022).

[2] K. Barlan, M. Cetera, and S. Horne-Badovinac, Fat2 and Lar define a basally localized planar signaling system controlling collective cell migration, Dev. Cell **40**, 467 (2017).

[3] P. A. Fernandez, B. Buchmann, A. Goychuk, L. K. Engelbrecht, M. K. Raich, C. H. Scheel, E. Frey, and A. R. Bausch, Surface-tension-induced budding drives alveologenesis in human mammary gland organoids, Nat. Phys. **17**, 1130 (2021).
[4] S. L. Haigo and D. Bilder, Global tissue revolutions in a morphogenetic movement controlling elongation, Science **331**, 1071 (2011).
[5] K. Sato, T. Hiraiwa, E. Maekawa, A. Isomura, T. Shibata, and E. Kuranaga, Left–right asymmetric cell intercalation drives directional collective cell movement in epithelial morphogenesis, Nat. Commun. **6**, 10074 (2015).
[6] T. H. Tan, A. Amiri, I. Seijo-Barandiarán, M. F. Staddon, A. Materne, S. Tomas, C. Duclut, M. Popović, A. Grapin-Botton, and F. Jülicher, Emergent chirality in active solid rotation of pancreas spheres, bioRxiv, 10.1101/2022.09.29.510101 (2022).
[7] A. S. Chin, K. E. Worley, P. Ray, G. Kaur, J. Fan, and L. Q. Wan, Epithelial cell chirality revealed by three-dimensional spontaneous rotation, Proc. Natl. Acad. Sci. U.S.A. **115**, 12188 (2018).
[8] E. Hirata, T. Ichikawa, S.-I. Horike, and E. Kiyokawa, Active K-RAS induces the coherent rotation of epithelial cells: A model for collective cell invasion *in vitro*, Cancer Sci. **109**, 4045 (2018).
[9] K. Tanner, H. Mori, R. Mroue, A. Bruni-Cardoso, and M. J. Bissell, Coherent angular motion in the establishment of multicellular architecture of glandular tissues, Proc. Natl. Acad. Sci. U.S.A. **109**, 1973 (2012).
[10] H. Wang, S. Lacoche, L. Huang, B. Xue, and S. K. Muthuswamy, Rotational motion during three-dimensional morphogenesis of mammary epithelial acini relates to laminin matrix assembly, Proc. Natl. Acad. Sci. U.S.A. **110**, 163 (2013).
[11] L. Happel, D. Wenzel, and A. Voigt, Effects of curvature on epithelial tissue—coordinated rotational movement and other spatiotemporal arrangements, Europhys. Lett. **138**, 67002 (2022).
[12] A. Glentis, C. Blanch-Mercader, L. Balasubramaniam, T. B. Saw, J. d'Alessandro, S. Janel, A. Douanier, B. Delaval, F. Lafont, C. T. Lim, D. Delacour, J. Prost, W. Xi, and B. Ladoux, The emergence of spontaneous coordinated epithelial rotation on cylindrical curved surfaces, Sci. Adv. **8**, eabn5406 (2022).
[13] S.-M. Yu, B. Li, F. Amblard, S. Granick, and Y.-K. Cho, Adaptive architecture and mechanoresponse of epithelial cells on a torus, Biomaterials **265**, 120420 (2021).
[14] L. Pieuchot, J. Marteau, A. Guignandon, T. Dos Santos, B. Isabelle, P. Chauvy, T. Cloatre, A. Ponche, T. Petithory, P. Rougerie, M. Vassaux, J.-L. Milan, N. Wakhloo, A. Spangenberg, M. Bigerelle, and K. Anselme, Curvotaxis directs cell migration through cell-scale curvature landscapes, Nat. Commun. **9**, 3995 (2018).
[15] M. Werner, A. Petersen, N. A. Kurniawan, and C. V. C. Bouten, Cell-perceived substrate curvature dynamically coordinates the direction, speed, and persistence of stromal cell migration, Adv. Biosyst. **3**, 1900080 (2019).
[16] N. D. Bade, T. Xu, R. D. Kamien, R. K. Assoian, and K. J. Stebe, Gaussian curvature directs stress fiber orientation and cell migration, Biophys. J. **114**, 1467 (2018).
[17] D. Baptista, L. Teixeira, C. van Blitterswijk, S. Giselbrecht, and R. Truckenmuller, Overlooked? Underestimated? Effects of substrate curvature on cell behavior, Trends Biotechnol. **37**, 838 (2019).
[18] S. J. P. Callens, R. J. C. Uyttendaele, L. E. Fratila-Apachitei, and A. A. Zadpoor, Substrate curvature as a cue to guide spatiotemporal cell and tissue organization, Biomaterials **232**, 119739 (2020).
[19] N. Harmand, A. Huang, and S. Henon, 3D shape of epithelial cells on curved substrates, Phys. Rev. X **11**, 031028 (2021).
[20] D. Bi, X. Yang, M. C. Marchetti, and M. L. Manning, Motility-driven glass and jamming transitions in biological tissues, Phys. Rev. X **6**, 021011 (2016).
[21] R. Farhadifar, J.-C. Roeper, B. Algouy, S. Eaton, and F. Jülicher, The influence of cell mechanics, cell-cell interactions, and proliferation on epithelial packing, Curr. Biol. **17**, 2095 (2007).
[22] M. Popovic, V. Druelle, N. A. Dye, F. Juelicher, and M. Wyart, Inferring the flow properties of epithelial tissues from their geometry, New J. Phys. **23**, 033004 (2021).
[23] B. A. Camley, Y. Zhang, Y. Zhao, B. Li, E. Ben-Jacob, H. Levine, and W.-J. Rappel, Polarity mechanisms such as contact inhibition of locomotion regulate persistent rotational motion of mammalian cells on micropatterns, Proc. Natl. Acad. Sci. U.S.A. **111**, 14770 (2014).
[24] J. Loeber, F. Ziebert, and I. S. Aranson, Collisions of deformable cells lead to collective migration, Sci. Rep. **5**, 9172 (2015).
[25] W. Marth and A. Voigt, Collective migration under hydrodynamic interactions: A computational approach, Interf. Focus **6**, 20160037 (2016).
[26] R. Mueller, J. M. Yeomans, and A. Doostmohammadi, Emergence of active nematic behavior in monolayers of isotropic cells, Phys. Rev. Lett. **122**, 048004 (2019).
[27] M. Nonomura, Study on multicellular systems using a phase field model, PLoS One **7**, e33501 (2012).
[28] B. Palmieri, Y. Bresler, D. Wirtz, and M. Grant, Multiple scale model for cell migration in monolayers: Elastic mismatch between cells enhances motility, Sci. Rep. **5**, 11745 (2015).
[29] D. Wenzel and A. Voigt, Multiphase field models for collective cell migration, Phys. Rev. E **184**, 054410 (2021).
[30] D. M. Sussman, Interplay of curvature and rigidity in shape-based models of confluent tissue, Phys. Rev. Res. **2**, 023417 (2020).
[31] G. Napoli and L. Vergori, Surface free energies for nematic shells, Phys. Rev. E **85**, 061701 (2012).
[32] G. Napoli and L. Vergori, Extrinsic curvature effects on nematic shells, Phys. Rev. Lett. **108**, 207803 (2012).
[33] M. Nestler, I. Nitschke, S. Praetorius, and A. Voigt, Orientational order on surfaces: The coupling of topology, geometry, and dynamics, J. Nonlinear Sci. **28**, 147 (2018).
[34] I. Nitschke, M. Nestler, S. Praetorius, H. Löwen, and A. Voigt, Nematic liquid crystals on curved surfaces: A thin film limit, Proc. R. Soc. A **474**, 20170686 (2018).
[35] D. Golovaty, J. Alberto Montero, and P. Sternberg, Dimension reduction for the Landau-de Gennes model on curved nematic thin films, J. Nonlinear Sci. **27**, 1905 (2017).

[36] M. Nestler, I. Nitschke, H. Löwen, and A. Voigt, Properties of surface Landau-de Gennes Q-tensor models, Soft Matter **16**, 4032 (2020).
[37] S. Bell, S.-Z. Lin, J.-F. Rupprecht, and J. Prost, Active nematic flows over curved surfaces, Phys. Rev. Lett. **129**, 118001 (2022).
[38] G. Napoli and S. Turzi, Spontaneous helical flows in active nematics lying on a cylindrical surface, Phys. Rev. E **101**, 022701 (2020).
[39] M. Nestler and A. Voigt, Active nematodynamics on curved surfaces-the influence of geometric forces on motion patterns of topological defects, Commun. Comput. Phys. **31**, 947 (2022).
[40] I. Nitschke, S. Reuther, and A. Voigt, Liquid crystals on deformable surfaces, Proc. R. Soc. A **476**, 20200313 (2020).
[41] H. P. Jain, A. Voigt, and L. Angheluta, Robust statistical properties of T1 transitions in a multi-phase field model of cell monolayers, Sci. Rep. **13**, 10096 (2023).
[42] D. Wenzel, S. Praetorius, and A. Voigt, Topological and geometrical quantities in active cellular structures, J. Chem. Phys. **150**, 164108 (2019).
[43] W. Marth, S. Praetorius, and A. Voigt, A mechanism for cell motility by active polar gels, J. R. Soc. Interface **12**, 20150161 (2015).
[44] D. Wenzel, M. Nestler, S. Reuther, M. Simon, and A. Voigt, Defects in active nematics—algorithms for identification and tracking, Comput. Meth. Appl. Math. **21**, 683 (2021).
[45] M. Salvalaglio, A. Voigt, and S. M. Wise, Doubly degenerate diffuse interface models of surface diffusion, Math. Meth. Appl. Sci. **44**, 5385 (2021).
[46] M. Benes, M. Kolar, J. M. Sischka, and A. Voigt, Degenerate area preserving surface Allen-Cahn equation and its sharp interface limit, arXiv:2303.04018.
[47] See Supplemental Material at http://link.aps.org/supplemental/10.1103/PhysRevLett.132.078401 for additional data and detailed descriptions on geometry, differential geometry, the full mathematical model, numerical issues, considered parameters and data analysis.
[48] L. Bai and D. Breen, Calculating center of mass in an unbounded 2D environment, J. Graphics Tools **13**, 53 (2008).
[49] K. Crane, C. Weischedel, and M. Wardetzky, Geodesics in heat: A new approach to computing distance based on heat flow, ACM Trans. Graph. **32**, 1 (2013).
[50] A. Doostmohammadi, J. Ignes-Mullol, J. M. Yeomans, and F. Sagues, Active nematics, Nat. Commun. **9**, 3246 (2018).
[51] G. Dziuk and C. M. Elliott, Finite element methods for surface PDEs, Acta Numer. **22**, 289 (2013).
[52] G. Peyret, R. Mueller, J. d'Alessandro, S. Begnaud, P. Marcq, R.-M. Mège, J. M. Yeomans, A. Doostmohammadi, and B. Ladoux, Sustained oscillations of epithelial cell sheets, Biophys. J. **117**, 464 (2019).
[53] R. Gu, X. Wang, and M. Gunzburger, Simulating vesicle-substrate adhesion using two phase field functions, J. Comput. Phys. **275**, 626 (2014).
[54] H. P. Jain, D. Wenzel, and A. Voigt, Impact of contact inhibition on collective cell migration and proliferation, Phys. Rev. E **105**, 034402 (2022).
[55] L. Shen, P. Lin, Z. Xu, and S. Xu, Thermodynamically consistent diffuse interface model for cell adhesion and aggregation, arXiv:2205.07190.
[56] B. Loewe, M. Chiang, D. Marenduzzo, and M. C. Marchetti, Solid-liquid transition of deformable and overlapping active particles, Phys. Rev. Lett. **125**, 038003 (2020).
[57] E. Vercurysse, D. B. Brückner, M. Gómez-González, M. Luciano, Y. Kalukula, L. Rossetti, X. Trepat, E. Hannezo, and S. Gabriele, Geometry-driven migration efficiency of minimal cell clusters, bioRxiv, 10.1101/2022.07.17.500364 (2022).
[58] D. Grossman, I. S. Aranson, and E. B. Jacob, Emergence of agent swarm migration and vortex formation through inelastic collisions, New J. Phys. **10**, 023036 (2008).
[59] A. M. Menzel and T. Ohta, Soft deformable self-propelled particles, Europhys. Lett. **99**, 58001 (2012).
[60] M. Nestler, I. Nitschke, and A. Voigt, A finite element approach for vector-and tensor-valued surface PDEs, J. Comput. Phys. **389**, 48 (2019).
[61] S. Praetorius and A. Voigt, Collective cell behavior—a cell-based parallelization approach for a phase field active polar gel model, in *NIC Symposium 2018*, edited by K. Binder, M. Müller, and A. Trautmann (Forschungszentrum Jülich GmbH, Zentralbibliothek, Jülich, 2018), Vol. 49, pp. 369–376.
[62] E. Bachini, V. Krause, I. Nitschke, and A. Voigt, Derivation and simulation of a two-phase fluid deformable surface model, J. Fluid Mech. **977** A41 (2023).
[63] P. Bastian, M. Blatt, A. Dedner, N.-A. Dreier, C. Engwer, R. Fritze, C. Gräser, C. Grüninger, D. Kempf, R. Klöfkorn, M. Ohlberger, and O. Sander, The Dune framework: Basic concepts and recent developments, Comput. Math. Appl. **81**, 75 (2021).
[64] P. Brandner, T. Jankuhn, S. Praetorius, A. Reusken, and A. Voigt, Finite element discretization methods for velocity-pressure and stream function formulations of surface Stokes equations, SIAM J. Sci. Comput. **44**, A1807 (2022).
[65] S. Praetorius and F. Stenger, Dune-CurvedGrid—A Dune module for surface parametrization, Arch. Num. Soft. **6**, 1 (2022).
[66] S. Vey and A. Voigt, AMDiS: Adaptive multidimensional simulations, Comput. Vis. Sci. **10**, 57 (2007).
[67] T. Witkowski, S. Ling, S. Praetorius, and A. Voigt, Software concepts and numerical algorithms for a scalable adaptive parallel finite element method, Adv. Comput. Math. **41**, 1145 (2015).
[68] V. Krause and A. Voigt, A numerical approach for fluid deformable surfaces with conserved enclosed volume, J. Comput. Phys. **486**, 112097 (2023).
[69] S. Reuther, I. Nitschke, and A. Voigt, A numerical approach for fluid deformable surfaces, J. Fluid Mech. **900**, R8 (2020).
[70] A. Torres-Sánchez, D. Millán, and M. Arroyo, Modelling fluid deformable surfaces with an emphasis on biological interfaces, J. Fluid Mech. **872**, 218 (2019).